# A systematic investigation into the effect of roughness on self-propelled swimming plates

**J. M. O. Massey[1]†, B. Ganapathisubramani[1] and G. D. Weymouth[1,2]**

[1]Faculty of Engineering and Physical Sciences, University of Southampton, UK
[2]Faculty of Mechanical, Maritime, and Materials Engineering, TU Delft, NL

(Received xx; revised xx; accepted xx)

This study examines the effects of surface topography on the flow and performance of a Self-Propelled Swimming (SPS) body. We consider a thin flat plate of length $L$ with an egg-carton roughness texture undergoing undulatory swimming kinematics at the typically observed biological Strouhal number of 0.3, amplitude to length ratio of 0.1, and Reynolds number of $12,000$. As the roughness wavelength, $\lambda$ is decreased, we find that the undulation wave speed $\zeta$ must be increased to maintain SPS. We find that large wavelength roughness results in the formation of horseshoe vortices around each element while smaller wavelengths result in large leading-edge vortices that dominate the flow field and the wake. Generally, increasing the wave speed $\zeta$ increases the power and side forces required to maintain SPS. However, when $\lambda \approx L/16$ there is a dramatic increase in the enstrophy (within the flow) that is not reflected in the forces on the body. The enstrophy increases when $\lambda$ is equivalent to the boundary layer thickness, a scaling known to amplify vorticity within the boundary layers. This indicates an interaction between the roughness and kinematics beyond a simple increase in viscous drag. Finally, we find that all but the longest roughness wavelength decreases the power required and reduces the RMS amplitude of the forces when compared to a smooth plate undergoing identical kinematics. This study reveals the nonlinear interaction between roughness and motion, illustrating that roughness studies on static shapes do not transfer directly to unsteady swimmers.

**Key words:** ...

## 1. Introduction

Underwater propulsion is an area of research that brings together engineers and biologists alike; it has fostered a deeper understanding of aquatic locomotion and inspired innovation in underwater systems. The kinematics have the most significant effect on the locomotive properties of marine animals; however, some intricacies of animal evolution, such as shark skin, have sparked research into the benefits of aquatic surface textures. Understanding the fluid dynamic interaction between kinematics and surface textures will help us to elucidate the contribution of surface textures to aquatic locomotion.

Previous work has identified important non-dimensional kinematic parameters for efficient swimming. The Strouhal number ($St$) describes the ratio between the product of the wake width and the shedding frequency, and the flow velocity, Triantafyllou *et al.* (1991, 1993) found that the optimal Strouhal number should be in the range $0.25 - 0.35$.

† Email address for correspondence: masseyjmo@gmail.com

Eloy 2012 tested the kinematics of fifty-three different types of fish based on Lighthill's elongated body theory (Lighthill 1960, 1971) and found that for high aspect-ratio tails, the optimal Strouhal number range was $0.2 - 0.4$. Saadat *et al.* (2017) showed that the Strouhal number was insufficient for efficient locomotion and defined a range of optimum motion amplitude to length ratio of 0.05 to 0.15. Di Santo *et al.* (2021) recently compared forty-four species of fishes and found that despite fishes' different morphologies categorised as; anguilliform, subcarangiform, carangiform, and thunniform, they shared a statistically significant oscillation amplitude, a.k.a kinematic envelope. This work is noteworthy as previous work suggested different kinematics were present depending on the morphology.

While kinematics have received the majority of the literature's attention, they are not the only factor affecting the locomotive properties of swimmers. Many studies have identified drag-reducing properties of certain textures. Although most of these studies are applied on static geometries, it has been suggested that these effects could transfer to unsteady aquatic propulsion. Bechert *et al.* (2000) showed that when the shark skin-like denticles interlock, they can passively reduce the drag on the surface much like a riblet. Riblets are small-scale two-dimensional transverse grooves whose height scale with the viscous scales of the flow and can act as drag reduction devices (Walsh (1982); Park & Wallace (1994); R García-Mayoral (2011); Cui *et al.* (2019)). However, if riblets are not viscous scaled and/or have other larger-scale features to them (such as a larger pattern of inclinations) they create new flow features and perhaps increase drag (Bechert *et al.* (2000); Nugroho *et al.* (2013); Von Deyn *et al.* (2022); Rouhi *et al.* (2022)). Similarly, When the denticles do not entirely interlock, the three-dimensionality of denticles can be detrimental and increase drag. The work of Boomsma & Sotiropoulos (2016) corroborated this finding; they compared two shapes of shark denticles to a scallop riblet design using DNS simulations. They found that the denticles increased the drag by $44\% - 50\%$ whilst the riblets reduced drag by 5% compared to the smooth surface. This suggests that there are issues related to the hydrodynamics of shark skin that remain unresolved.

During a swim cycle, riblets might briefly overlap at the drag-reducing viscous scales set out by Bechert *et al.* (2000) however, the morphing of the body and the fluctuating viscous length scales force the denticles outside of the conditions that cause riblets to decrease drag the majority of the time. To comprehend the potential hydrodynamic benefit of shark skin or other similar surface textures, we must look at it in the context of a larger, dynamic system. Studies suggest that shark skin uses passive control in the flank region to bristle the skin while swimming, increasing boundary layer mixing and helping to keep the flow attached at areas of flow reversal (Lang *et al.* 2008; Afroz *et al.* 2016; Santos *et al.* 2021). Oeffner & Lauder (2012) tested samples of skin from the midsection of a short-fin mako shark on both a rigid flapping plate and a flexible plate. They found that the skin actually reduced the rigid plate's propulsive effectiveness. They also found that adding shark skin increased the flexible plate's swimming speed by 12%. However, they do not provide the amplitude envelope for the flexible plate which would ensure constant kinematics between the cases tested. Similarly, Wen *et al.* (2014) covered an undulating plate in 3D printed denticles of $100\times$ actual size and measured a 6.6% efficiency increase. Again, they do not provide an amplitude envelope to ensure the kinematics between the smooth and the rough surfaces remain constant. The denticles in the above-mentioned work (Oeffner & Lauder (2012); Wen *et al.* (2014)) are not scaled with local viscous scales so that they are within the drag-reducing regimes set out by Bechert *et al.* (2000). Therefore, the physical mechanisms responsible for the differences between rough and smooth surfaces remain unclear and illustrates the need for a systematic study to examine the interaction between surface textures and kinematics.

The complex and multi-scale shape of denticles does not lend itself to systematic investigations into the interplay between surface textures and kinematics. Consequently, we look to simplify the surface texture. We need to span a relevant parameter space and yet ensure that the parameterisation of the surface is suited for the proposed problem. We look for inspiration in the surface textures/geometries that have been explored in previous studies that have focused on developing methods for predicting drag on flow over rough surfaces (Moody (1944); Jiménez (2004); Flack & Schultz (2010, 2014); García-Mayoral *et al.* (2019); Chung *et al.* (2021)). Previous studies have indicated that the ratio of the total projected frontal roughness area to the wall-paralleled projected area (solidity, $\Lambda$, Schlichting 1936) and the mean slope of the roughness texture (in the streamwise and spanwise directions, also known as effective slope, $ES$, Napoli *et al.* 2008) are two geometric parameters of a rough surface known to significantly affect the flow and forces. These two parameters can be easily altered for structured surfaces where the surface geometry has a sinusoidal shape. In fact, previous works have used sinusoidal roughness where the variation of the two roughness properties can be achieved by only altering the wavelength of the sinusoidal shape (Napoli *et al.* 2008; Chan *et al.* 2015; Ma *et al.* 2020; Ganju *et al.* 2022). This presents us with a surface that can be used to understand how the primary scales of roughness (parameterised by a single quantity) interacts with kinematics, with the hope that the findings can be generalised to more complex geometries.

In this work, we study the interaction between kinematics and roughness topologies through high-resolution simulations of a rough self-propelled swimming thin plate. We fix the Reynolds number ($Re$) of these simulations to $12,000$ (based on swimming speed and chord length) to access moderate Reynolds numbers for these types of flows that are in line with previous efforts (Oeffner & Lauder (2012); Wen *et al.* (2014); Domel *et al.* (2018)). We also fix the kinematics of the plate to a simple travelling waveform with a fixed Strouhal number, $St$, that is in the propulsive regime for flapping foils and has been used extensively in previous studies (Maertens & Weymouth (2015); Muscutt *et al.* (2017); Zurman-Nasution *et al.* (2020)). As denticle geometries are complex with several potentially important length scales, we focus on a simple roughness texture with a single-length scale to assess how the topology interacts with the kinematics and impacts the hydrodynamic properties of the swimmer. By combining information from two different, but, well-established topics we hope to understand the influence of one on the other. These dynamic simulations with roughness elements are the first of their kind allowing us first to establish a link between surface roughness and kinematics, and then, with comparison to a smooth kinematic counterpart, to directly isolate the nonlinear interaction of the roughness and kinematics.

## 2. Methodology

### 2.1. *Geometry*

We use a flat plate with a thickness 3% of the plate length $L$ as the base model. Using a flat plate couples the dynamics and the surface texture in the simplest possible setup, similar to thin aerofoil theory. Using a body with curvature would also make some bumps more proud to the flow than others, changing the effective amplitude of the bumps along the body. A thin plate enables the use of a constant bump amplitude $h$ of 1% of the plate length all along the body.

For the roughness, we use a sinusoidal roughness, similar to Napoli *et al.* (2008); Chan *et al.* (2015); Ma *et al.* (2020); Ganju *et al.* (2022), that allows us to vary the

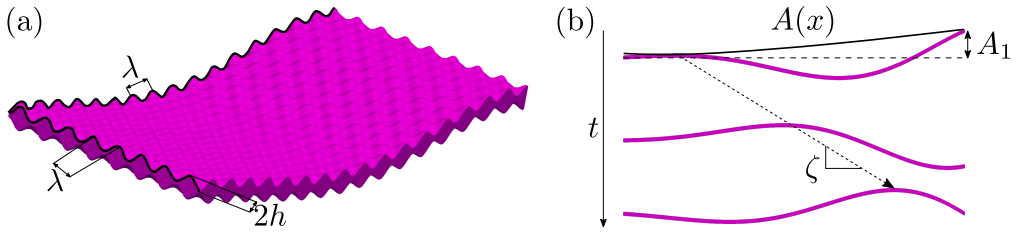


Figure 1: (a), the geometry used, which has two defining parameters $\lambda$, the wavelength of the roughness, and $h$, the roughness amplitude. (b), a visual representation of the parameters that define the plate motion.

roughness topology systematically. Figure 1a illustrates the parameters affecting the roughness topology. Normalising all lengths by the plate length $L$, the topography is defined as

$$y(x,z) = \begin{cases} h\sin\left(\frac{2\pi x}{\lambda}\right)\cos\left(\frac{2\pi z}{\lambda}\right), & \text{for } y \geqslant 0.015 - h \\ h\sin\left(\frac{2\pi x}{\lambda} - \pi\right)\cos\left(\frac{2\pi z}{\lambda}\right), & \text{for } y \leqslant -0.015 + h \end{cases} \tag{2.1}$$

where $y$ is the direction normal to the plate and $x, z$ are the tangential direction, and $\lambda$ is the roughness wavelength.

### 2.2. *Kinematics*

Continuing to scale all lengths by $L$, using the swimming speed $U$ to scale velocity and $L/U$ to scale time, we define the excursion of the body from the centre line as

$$y(x) = A(x)\sin\left(2\pi f\left[t - x/\zeta\right]\right) \tag{2.2}$$

where $f$ is the frequency, $\zeta$ is the phase speed of the travelling wave, and $A(x)$ is the amplitude envelope, all of which are illustrated in figure 1b. The Strouhal number is set to peak propulsive value $St = 0.3$ which determines the scaled frequency as $f = St/A_1$, where $A_1 = A(x = 1)$ is the trailing edge amplitude. We modify the recent result from Di Santo *et al.* 2021 for the envelope

$$A(x) = a_2 x^2 + a_1 x + a_0 \tag{2.3}$$

using $a_{0,1,2} = (0.05, 0.13, 0.28)$ such that $A_1 = 0.1$, as found to be optimal in Saadat *et al.* 2017.

### 2.3. *Numerical Method*

We simulate incompressible fluid flow with the dimensionless Navier-Stokes equation combined with the continuity equation

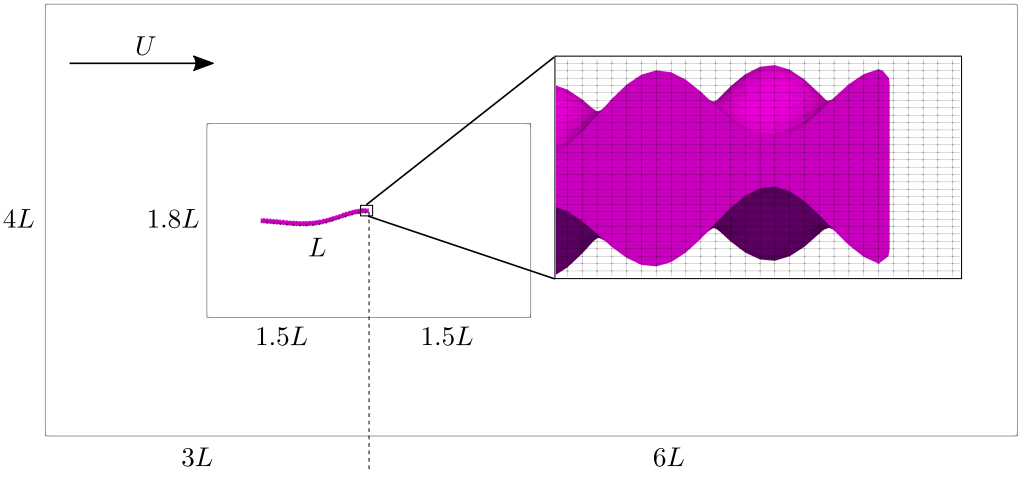


Figure 2: The position and domain. The inner box shows the region where the grid is uniformly rectilinear; from there, the grid stretches toward the domain extent. This is the grid for $\lambda = 1/16$; the total domain is $(9, 4, 8\lambda)L$ totalling 302 million grid cells. There is a periodic condition in the spanwise direction $z$, so when $\lambda$ varies, the spanwise extent changes to ensure the surface wave is continuous. We use the closest number of wavelengths so that the spanwise distance is $\approx 0.5L$. The insert indicates the grid around the tail of the plate.

$$\frac{\partial \vec{u}}{\partial t} + (\vec{u} \cdot \vec{\nabla})\vec{u} = -\vec{\nabla} p + \frac{1}{Re}\nabla^2 \vec{u} \tag{2.4}$$

$$\vec{\nabla} \cdot \vec{u} = 0. \tag{2.5}$$

where $\vec{u}(\vec{x}, t) = (u, v, w)$ is the scaled velocity of the flow, and $p(\vec{x}, t)$ is the scaled pressure.

The undulating plate was coupled to these flow equations using the Boundary Data Immersion Method (BDIM) formulated in Weymouth & Yue (2011) and further developed for higher Reynolds numbers in Maertens & Weymouth (2015) and thin geometries in Lauber *et al.* (2022). BDIM enforces the boundary condition on the body by convolving together the fluid and body governing equations on a Cartesian background grid. BDIM has been extensively validated in those studies and converges at second order in both time and space.

Figure 2 details the grid and domain set-up. We used the smallest domain for which the forces on the body remained invariant when the size increased. We define the force and power coefficients as

$$C_T = \frac{\oint \vec{f}_x ds}{0.5S}, \quad C_L = \frac{\oint \vec{f}_y ds}{0.5S}, \quad C_P = \frac{\oint \vec{f} \cdot \vec{v} ds}{0.5S} \tag{2.6}$$

where $\vec{f} = -p\hat{n}$ is the normal pressure stress on the body, $\vec{v}$ is the body velocity, and $S$ is the planform area of the smooth plate. Careful consideration of the aspect ratio of the maximum cell meant that it did not exceed five times that of the uniform region downstream to avoid distorting the flow in the wake. We present the grid convergence results in Appendix A.

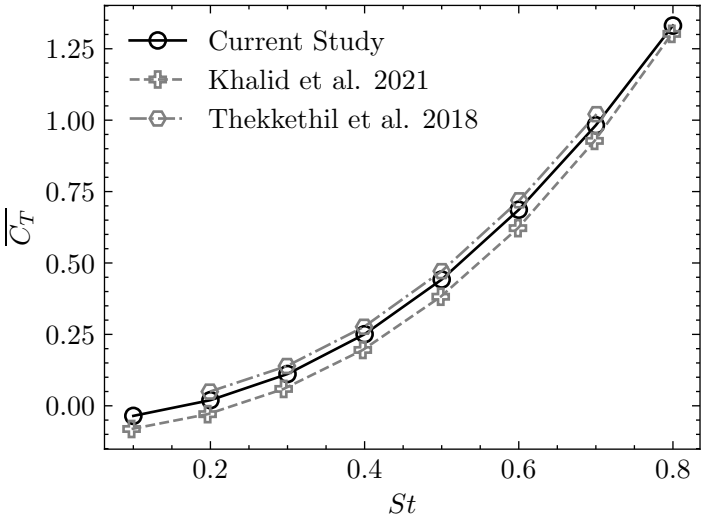


Figure 3: A comparison of the $\overline{C_T}, St$ relationship from Thekkethil *et al.* (2018) and Khalid *et al.* (2021) with the current study. For all cases $\zeta = 1.5$ and $Re = 5,000$. The geometry and amplitude envelope differ between the cases and accounts for the differences.

To show that our method is consistent with other swimming studies, we have compared the $St, \overline{C_t}$ plot against Thekkethil *et al.* (2018) and Khalid *et al.* (2021) (figure 3). In this figure have matched $Re = 5,000$ and set $\zeta = 1.5$ but kept our flat plate geometry, and the kinematics described. Thekkethil *et al.* (2018) used a NACA0012 profile and considers a linear amplitude envelope, Khalid *et al.* (2021) uses a quadratic amplitude envelope and a foil shape. There is minimal variation in the thrust coefficient despite the differences in kinematics and geometry, which shows the suitability of our model using a flat plate. For a more detailed validation of BDIM for swimming simulations, the reader is referred to Maertens *et al.* (2017) who performs a like-for-like comparison of undulatory locomotion with Dong & Lu (2007).

## 3. Results

### 3.1. *Self-Propelled Swimming*

We find the Self-Propelled Swimming (SPS) state by setting the wave speed $\zeta$ to zero the mean thrust $\overline{C_T}$. The wave speed is an effective control parameter to counter roughness adjustments because increasing $\zeta$ increases the thrust production, as shown for a smooth plate in figure 4b. Figure 4a illustrates the change in body shape as the wave speed increases. Changing $\zeta$ to achieve SPS allows us to keep $Re$, $St$ and $A_1$ constant to test different surface conditions without changing these important swimming parameters identified in the literature. We use Brent's method to find the $\overline{C_T}(\zeta) = 0$ root within a tolerance of $10^{-2}$ which allows us to balance precision with the number of iterations.

Using this approach, we found that a decrease in the roughness wavelength $\lambda$ requires an increase of $\zeta$ to maintain SPS, figure 4c. $\zeta$ changes with $\lambda$ like the function $\frac{1}{|\lambda|} + c$ (figure 4c). The $\zeta, \lambda$ relationship leads us to restrict $\lambda$ in the range $(1/4, 1/52)$ as the limits are ill-conditioned. Longer wavelengths asymptote to the smooth SPS ($\zeta = 1.06$) where $\lambda \equiv 1/0$ whilst all $\lambda < 1/52$ are drag-producing for our set-up.

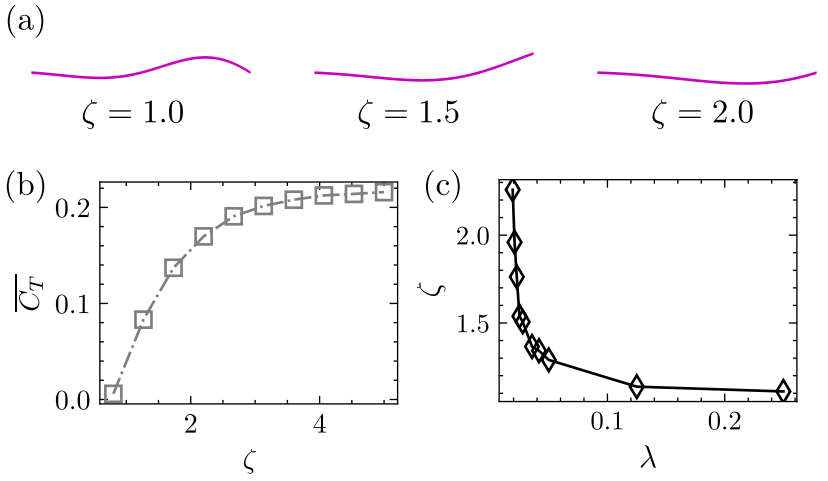


Figure 4: The impact of $\zeta$ to shape, forces, and SPS roughness. (a) Illustrated body shapes for different values of $\zeta$. (b) Dependence of $\overline{C_T}$ as a function of $\zeta$ for a smooth undulating plate. (c) The required wave speeds $\zeta$ for SPS of a rough plate given different wavelengths $\lambda$.

### 3.2. *Flow Structures*

Figure 5 shows equally spaced time instances making up a whole period of motion for two different swimming modes. One swimming mode is $\zeta = 1.11$ which is required to achieve SPS for a surface of $\lambda = 1/4$, the other is $\zeta = 2.27$ for $\lambda = 1/52$. The high wave speed required to overcome roughness has resulted in strong coherent vortices whilst the lower wave speed has a much more dispersed vorticity field.

As $\zeta$ increases, the flow around the plate moves away from those typically associated with swimming. Figure 6 shows four snapshots across the range of $\zeta$ associated with the surfaces tested. (a) is a smooth comparison and exhibits a two-pair plus two-single ($2P + 2S$) vortex wake structure (Schnipper *et al.* 2009). For (b), there is an increase in the boundary layer mixing, and the flow moves back to a more traditional 2P structure. As $\lambda$ decreases further, the leading edge vortex becomes more defined, with (c) and (d) exhibiting well-defined vortices along the length of their body which is generally associated with a heaving instead of a swimming plate

Figure 7 shows the flow structure visualised by isosurfaces of the Q-Criterion (Hunt *et al.* 1988). For a direct comparison, the contour of the isosurface remains the same between the figures. The flow exhibits a distinguishable transition as $\zeta$ increases. For low $\zeta$ the bumps dominate the flow structure, and we see distinct horseshoe vortices shed from each element. These vortices persist downstream into counter-rotating streaks that compose the near wake. The flow structures get smaller as $\zeta$ increases and the horseshoe vortex around each element becomes less distinct. From the middle left figure onwards, we can see the near wake collects into a wavy vortex tube similar to those that categorise a two-dimensional flow driven by kinematics Zurman-Nasution *et al.* (2020).

### 3.3. *Forces*

We find that increasing $\zeta$ increases the power to maintain SPS (figure 8a) despite the strong two-dimensionality of the flow structures which are normally associated with efficient power transfer as no energy is lost to three-dimensional effects. This means low $\zeta$

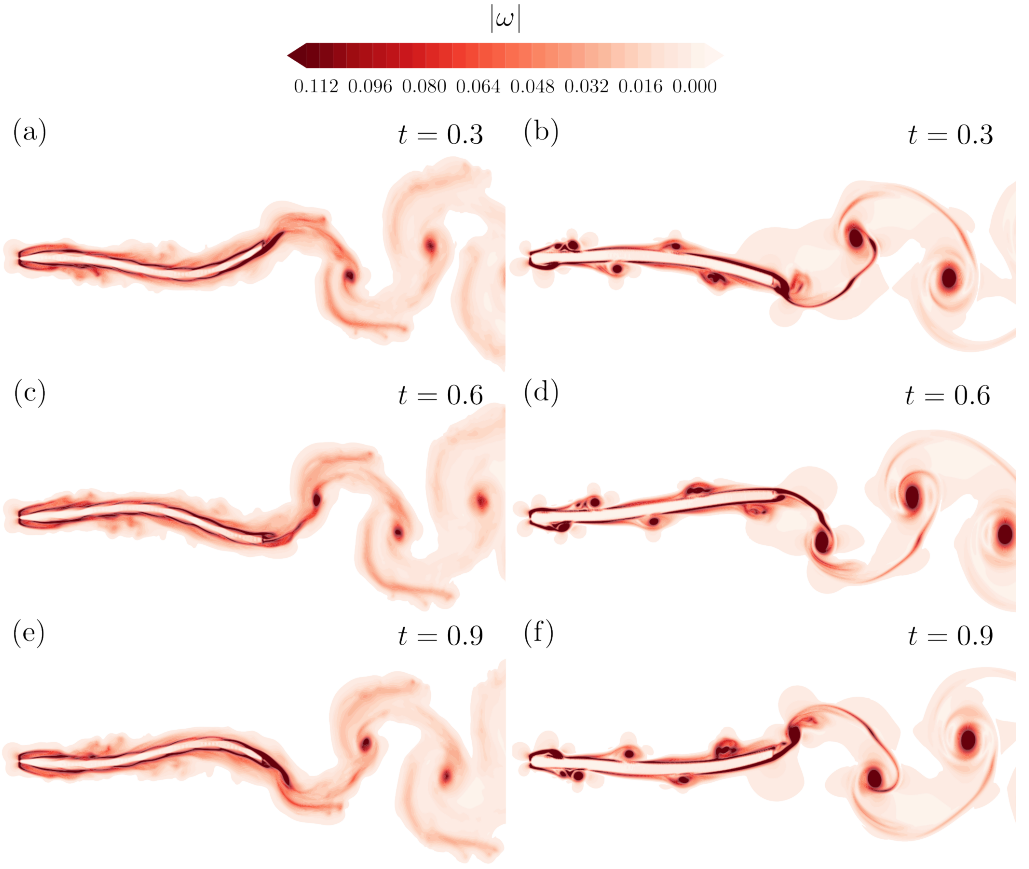


Figure 5: A sequence of snapshots of vorticity magnitude $|\omega|$. The two columns represent different roughness wavelengths, (a,c,d) $\lambda = 1/4$ requiring $\zeta = 1.11$ for SPS, and (b,d,e) $\lambda = 1/52$ requiring $\zeta = 2.27$.

corresponding to the longer wavelength roughness and associated three-dimensional flow structures are more efficient.

Figure 2.3b show that as $\zeta$ increases, as does $RMS(C_L)$. This signals ineffective swimming as the side forces are balanced by the mass $\times$ acceleration of the body's motion so larger side forces on an equally massive body cause the body to accelerate side to side more, decreasing the smoothness. Similarly, increasing $\zeta$ also increases $RMS(C_T)$ (figure 2.3d) leading to more of a surging motion, further decreasing the smoothness of the swimming. These signs of ineffective swimming are reflected in the stated increase in $\overline{C_P}$.

To decouple the roughness and wave speed effects, we run a smooth simulation with the same kinematics properties as each rough case. The smooth kinematic counterpart gives a base flow to compare against the rough simulations, and the cycled average power and forces are shown in Figure 8. Figure 8c illustrates that increasing $\zeta$ for the smooth case increases $\overline{C_T}$, making the smooth-plate counterparts slightly thrust producing. However, the $\overline{C_T}$ produced by the smooth plate is small enough that the flow regime doesn't change significantly, making them directly comparable to the rough Self-Propelled Swimming cases. The power $\overline{C_P}$ is reduced by adding roughness to the surface of the plate, Figure

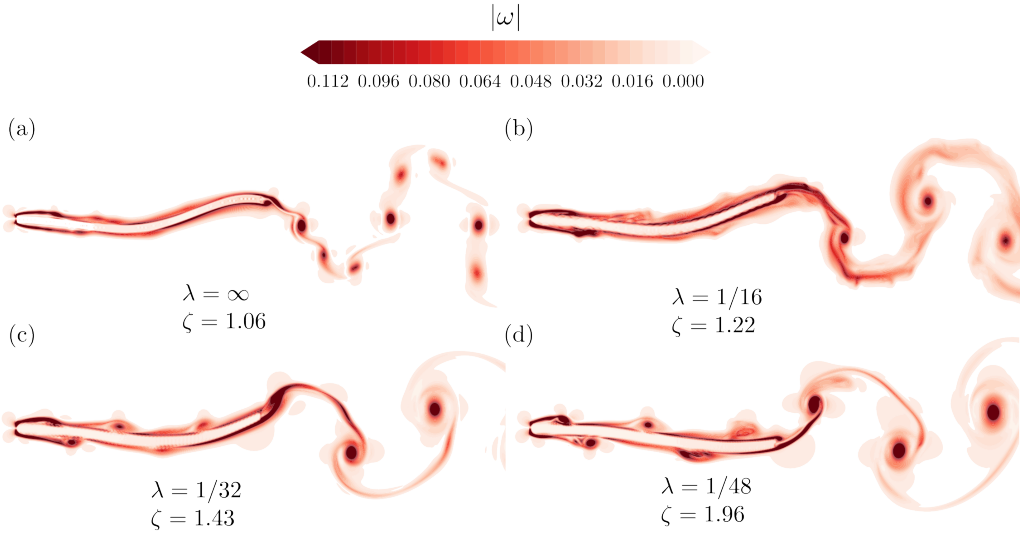


Figure 6: Illustrations of the change in vorticity magnitude as roughness wavelength changes. All instances are taken at the same cycle time $t = 0.1$ and show the phase average over four cycles of the spanwise averaged vorticity magnitude. (a) is a smooth plate and (b-d) are roughnesses with decreasing $\lambda$.

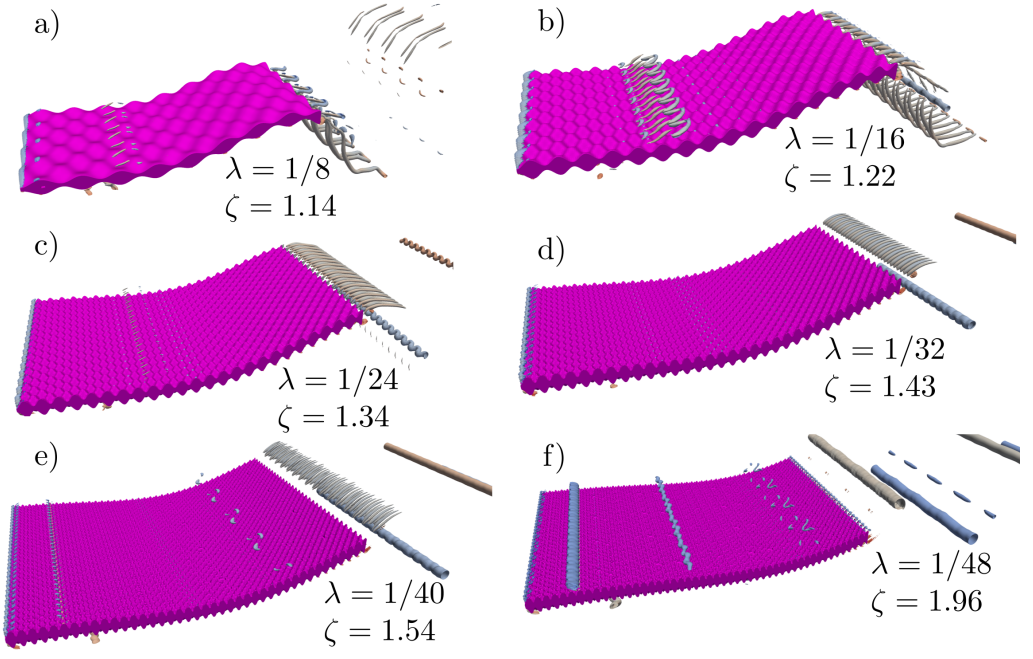


Figure 7: This figure shows the Q-Criterion of the flow around a flat plate with a decreasing roughness wavelength. For longer wavelength roughness, the bumps dominate the structures, but as the wavelength decreases, the flow transitions to a two-dimensional state.

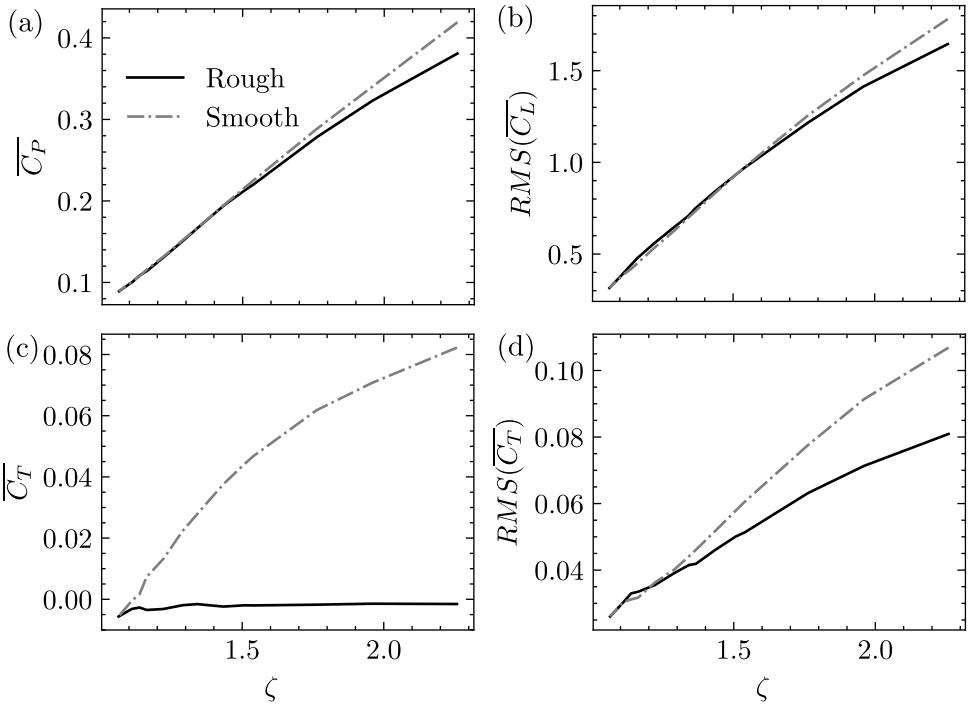


Figure 8: This figure shows the key swimming performance and force characteristics of the plate. The power required to maintain SPS (a). The side force RMS (b). The time-averaged (c) and RMS (d) thrust. The points making up the black line are the rough simulations and the grey line is a kinematically equivalent smooth simulation which matches $\zeta$ to the rough case.

8a, for the shorter wavelength roughnesses tested. Shorter wavelength roughness also reduces $RMS(C_L)$ (figure 8b) and $RMS(C_T)$ (figure 8d), making the swimming more effective compared to a smooth, kinematic counterpart.

### 3.4. *Enstrophy*

So far, we have shown surface roughness increases the drag on a surface, leading to inefficient swimming, and have identified variations in the flow structures for different textures and kinematics. To identify the separate fluid dynamic contribution of $\zeta$ and $\lambda$ we look at scaled enstrophy of the rough surface and its smooth kinematic counterpart. We define the scaled enstrophy as

$$E = \frac{\int 0.5|\omega|^2 dV}{SA_1} \tag{3.1}$$

where the scaling factor is the planform area times the motion amplitude to define an appropriate reduced volume over which to evaluate the mixing.

Figure 9a shows the results of $E$ against $\zeta$, where the black line are the rough plate results and the grey line are the smooth, kinematic counterparts. The positive gradient of both the lines shows that increasing $\zeta$ increases enstrophy, and the offset between the grey and the black line indicates that adding roughness also increases enstrophy. As we increase $\zeta$, the enstrophy increases for both the smooth and the rough cases. At the

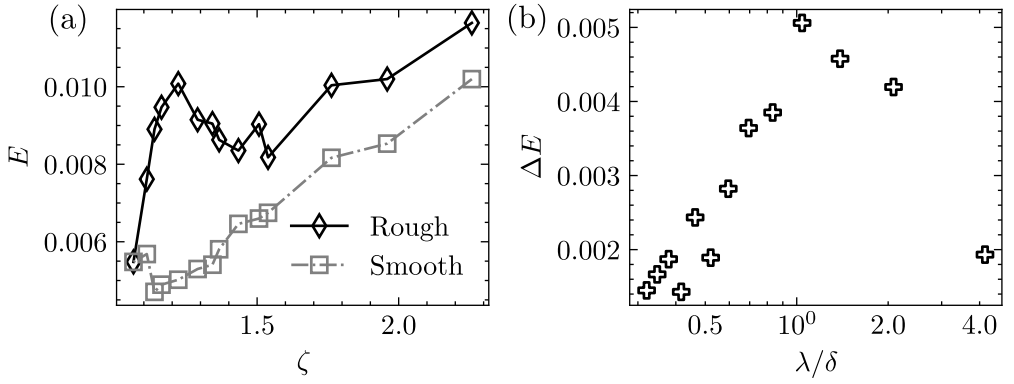


Figure 9: (a), the enstrophy ($E$) of the system depending on $\zeta$ of the plate. The black line is the rough plate with decreasing $\lambda$ and the grey line is a smooth plate with identical kinematics. (b), the difference between the smooth and the rough $E$ scaled by $\lambda/\delta$ where $\delta$ is the accelerated boundary layer thickness on the smooth plate.

upper limit of $\zeta$, the smooth and the rough lines start converging as the rough, like the smooth, flow becomes two-dimensional (figure 7).

One prominent feature of figure 9a is the peak in enstrophy at $\zeta \approx 1.2$ corresponding to a roughness wavelength $\lambda = 1/16$. The peak in enstrophy coincides with the superposition of the flow features associated with both the roughness and kinematics (figure 7b). This is evident as surfaces with shorter $\lambda$ are increasingly dominated by the two-dimensional vortex tubes associated with the kinematic flow as the structures shed off the roughness elements decrease in size (figure 7c-f), and surfaces with longer $\lambda$ are dominated by the flow off the the roughness elements (figure 7b).

We can relate this peak in enstrophy to an amplification of turbulent flow structures similar to those found in Prandtl's Secondary Motions of the Second Kind (Johann Nikuradse 1926; Ludwig Prandtl 1926) where secondary currents were induced when the surface texture has features that scale with the outer length-scale of the flow. In fact, Hinze (1967, 1973) found that when surface roughness has dominant scales that are comparable to the boundary layer thickness (or pipe/channel height, then, there is an imbalance between turbulence production and dissipation (locally) leading to the presence of secondary currents. These secondary currents manifest as low and high-momentum pathways in the flow (Barros & Christensen 2014) that are further sustained by spatial gradients (Anderson *et al.* 2015). Vanderwel & Ganapathisubramani (2015) identified that the spatial gradients and the strength of these secondary currents are maximised when the spanwise spacing between successive roughness features are approximately equal to the boundary layer thickness. When, the spacing is small, the the flow behaves more like a homogeneous rough surface and when the spacing is much larger then the secondary motions are spatially confined (and small) to the location of the roughness.

In figure 9b we plot the difference in enstrophy between the smooth and the rough plate ($\Delta E$) against $\lambda/\delta$ where $\delta = 0.06$ is the average accelerated boundary layer height at the trailing edge of the smooth plate. The peak in $\Delta E$ occurs when $\lambda/\delta \approx 1$. For smaller and larger values of this ratio, the enstrophy differences are smaller. In fact, estimating the value of $\delta$ by assuming a turbulent boundary layer correlation ($\delta/x \approx 0.38 {Re_x}^{-0.2}$) also yields a result where $\lambda = 1/16$ corresponds to $\lambda/\delta \approx 1$. Therefore, it might be possible for future studies to assess the importance of their dominant roughness length scale based

on this type of estimation. Finally, in our study, the power increases almost linearly until $\zeta \approx 1.8$, figure 8a and our enstrophy peak lies within this regime. This means that the accentuation of these secondary flows truly is a boundary layer scaling, and not a result of increased vorticity production at the wall (due to kinematics). Therefore, we can relate the system's increase in mixing to scaling arguments previously defined in turbulent wall-flows.

## 4. Conclusion

In this paper, we examined the effect of an egg-carton-type rough surface on a Self Propelled Swimming Body. We varied the wavelength of the surface to understand how different surface topologies change the flow and performance of the swimmer. We found a decrease in the roughness wavelength requires an increase in the wave speed to maintain SPS. Increasing the wave speed changed the vortex structures and consolidated the vorticity into two-dimensional packets with a distinct leading edge vortex propagating down the body. The long wavelength rough surfaces are dominated by horseshoe vortices shed off individual roughness elements and persisted in the wake. Increasing the wave speed increased the thrust, which was needed to overcome the drag induced by the roughness, but also increased the required power and the amplitude of the non-propulsive lift force. These increases implied the plate was less efficient, less effective, and less steady in its swimming. To decouple the effects of roughness and kinematics we compared the forces and enstrophy to a smooth swimmer with identical kinematics. We saw that, compared to the smooth cases, the roughness reduced the power required, as well as the amplitude of the lift, and drag forces. There was a peak in enstrophy which coincided with a superposition of two flow modes, one dominated by three-dimensional structures and the other by the two-dimensional tubes. The peak in enstrophy was observed when the roughness wavelength matches the boundary layer thickness which is in line with scaling arguments defined for turbulent wall-flows (Vanderwel & Ganapathisubramani 2015).

These results show that you cannot ignore kinematics when assessing the performance of a swimmer with surface texture. Oeffner & Lauder (2012) and Wen *et al.* (2014) reported an increase in speed and efficiency for their experiments but we have shown a change in wave speed dominates the thrust production of the plate. Adding a coating to a surface could increase the stiffness and hence wave speed, causing the plate to swim faster. Another factor to consider is the structural resonance which significantly affects the performance of flexible plates undergoing swimming (Quinn *et al.* 2014). Any study attributing performance changes to surface textures must show the independence of their test cases to the kinematics.

We have identified non-linear interactions between the roughness and kinematics that amplify this mixing without a nonlinear force or power increase. Other studies (Lang *et al.* 2008; Afroz *et al.* 2016; Santos *et al.* 2021) have identified the bristling of shark skin and conjectured that the increased mixing helps keep flow attached in the flank region. This work is significant in understanding the hydrodynamic effect of surface textures on the flow and forces around a swimmer, it is the first study to look at surface textures on undulating surfaces with realistic and well-defined kinematics. However, it is limited in that the roughness elements are a hundred times larger than actual denticles, and $Re$ is under-sampled and only representative of a small, slow-swimming shark.

## Acknowledgements

We would like to thank the IRIDIS high performance computing facility and it's associated support at the University of Southampton, the Office of Naval Research Global Award N62909-18-1-2091.

## Declaration of Interests

The authors report no conflict of interest.

## REFERENCES

Afroz, Farhana, Lang, Amy, Habegger, Maria Laura, Motta, Philip & Hueter, Robert 2016 Experimental study of laminar and turbulent boundary layer separation control of shark skin. *Bioinspiration & biomimetics* **12** (1), 16009.

Anderson, William, Barros, Julio M., Christensen, Kenneth T. & Awasthi, Ankit 2015 Numerical and experimental study of mechanisms responsible for turbulent secondary flows in boundary layer flows over spanwise heterogeneous roughness. *Journal of Fluid Mechanics* **768**, 316–347.

Barros, Julio M. & Christensen, Kenneth T. 2014 Observations of turbulent secondary flows in a rough-wall boundary layer. *Journal of Fluid Mechanics* **748** (2), R1.

Bechert, D W, Bruse, M & Hage, W 2000 Experiments with three-dimensional riblets as an idealized model of shark skin. *Experiments in fluids* **28** (5), 403–412.

Boomsma, A & Sotiropoulos, F 2016 Direct numerical simulation of sharkskin denticles in turbulent channel flow. *Phys. Fluids* **28**, 35106.

Chan, L, Macdonald, M, Chung, D, Hutchins, N & Ooi, A 2015 A systematic investigation of roughness height and wavelength in turbulent pipe flow in the transitionally rough regime. *J. Fluid Mech* **771**, 743–777.

Chung, Daniel, Hutchins, Nicholas, Schultz, Michael P. & Flack, Karen A. 2021 Predicting the Drag of Rough Surfaces. *https://doi.org/10.1146/annurev-fluid-062520-115127* **53**, 439–471.

Cui, Guangyao, Pan, Chong, Wu, Di, Ye, Qingqing & Wang, Jinjun 2019 Effect of drag reducing riblet surface on coherent structure in turbulent boundary layer. *Chinese Journal of Aeronautics* **32** (11), 2433–2442.

Di Santo, Valentina, Goerig, Elsa, Wainwright, Dylan K, Akanyeti, Otar, Liao, James C, Castro-Santos, Theodore & Lauder, George V 2021 Convergence of undulatory swimming kinematics across a diversity of fishes. *Proceedings of the National Academy of Sciences of the United States of America* **118** (49).

Domel, August G., Saadat, Mehdi, Weaver, James C., Haj-Hariri, Hossein, Bertoldi, Katia & Lauder, George V. 2018 Shark skin-inspired designs that improve aerodynamic performance. *Journal of the Royal Society Interface* **15** (139), 1–9.

Dong, Gen Jin & Lu, Xi Yun 2007 Characteristics of flow over traveling wavy foils in a side-by-side arrangement. *Physics of Fluids* **19** (5), 057107.

Eloy, Christophe 2012 Optimal Strouhal number for swimming animals. *Journal of Fluids and Structures* **30**, 205–218.

Flack, Karen A. & Schultz, Michael P. 2010 Review of hydraulic roughness scales in the fully rough regime. *Journal of Fluids Engineering, Transactions of the ASME* **132** (4), 0412031–04120310.

Flack, Karen A. & Schultz, Michael P. 2014 Roughness effects on wall-bounded turbulent flowsa). *Physics of Fluids* **26** (10), 101305.

Ganju, Sparsh, Bailey, Sean C.C. & Brehm, Christoph 2022 Amplitude and wavelength scaling of sinusoidal roughness effects in turbulent channel flow at fixed. *Journal of Fluid Mechanics* **937**, A22.

García-Mayoral, R., Gómez-De-Segura, G. & Fairhall, C. T. 2019 The control of near-wall turbulence through surface texturing. *Fluid Dynamics Research* **51** (1), 011410.

Hinze, J. O. 1967 Secondary Currents in Wall Turbulence. *The Physics of Fluids* **10** (9), S122.

Hinze, J. O. 1973 Experimental investigation on secondary currents in the turbulent flow through a straight conduit. *Applied Scientific Research 1973 28:1* **28** (1), 453–465.

Hunt, J. C. R., Wray, A. A., Moin, P., Wray, A. A. & Moin, P. 1988 eddies, streams, and convergence zones in turbulent flows. *Studying Turbulence Using Numerical Simulation Databases, 2. Proceedings of the 1988 Summer Program* .

Jiménez, Javier 2004 Turbulent flows over rough walls. *Annual Review of Fluid Mechanics* **36** (1991), 173–196.

Johann Nikuradse 1926 Untersuchung über die Geschwindigkeitsverteilung. *ZAMM - Journal of Applied Mathematics and Mechanics / Zeitschrift für Angewandte Mathematik und Mechanik* **6** (6), 503–503.

Khalid, Muhammad Saif Ullah, Wang, Junshi, Akhtar, Imran, Dong, Haibo, Liu, Moubin & Hemmati, Arman 2021 Why do anguilliform swimmers perform undulation with wavelengths shorter than their bodylengths? *Physics of Fluids* **33** (3), 031911.

Lang, A W, Motta, P, Hidalgo, P & Westcott, M 2008 Bristled shark skin: a microgeometry for boundary layer control? *Bioinspiration & biomimetics* **3** (4), 46005.

Lauber, Marin, Weymouth, Gabriel D & Limbert, Georges 2022 Immersed Boundary Simulations of Flows Driven by Moving Thin Membranes. *Physics of Fluids* .

Lighthill, M. J. 1960 Note on the swimming of slender fish. *Journal of Fluid Mechanics* **9** (2), 305–317.

Lighthill, M J 1971 Large-amplitude elongated-body theory of fish locomotion. *Proceedings of the Royal Society of London. Series B. Biological Sciences* **179** (1055), 125–138.

Ludwig Prandtl 1926 Über die ausgebildete Turbulenz. *Verhandl. des II. Int. Kongr. für Techn. Mech.* pp. 62–75.

Ma, Guo Zhen, Xu, Chun Xiao, Sung, Hyung Jin & Huang, Wei Xi 2020 Scaling of rough-wall turbulence by the roughness height and steepness. *Journal of Fluid Mechanics* **900**.

Maertens, Audrey P., Gao, Amy & Triantafyllou, Michael S. 2017 Optimal undulatory swimming for a single fish-like body and for a pair of interactingÂ swimmers. *Journal of Fluid Mechanics* **813**, 301–345.

Maertens, Audrey P. & Weymouth, Gabriel D. 2015 Accurate Cartesian-grid simulations of near-body flows at intermediate Reynolds numbers. *Computer Methods in Applied Mechanics and Engineering* **283**, 106–129.

Moody, Lewis F 1944 Friction factors for pipe flow. *Trans. Asme* **66**, 671–684.

Muscutt, L. E., Weymouth, G. D. & Ganapathisubramani, B. 2017 Performance augmentation mechanism of in-line tandem flapping foils. *Journal of Fluid Mechanics* **827**, 484–505.

Napoli, E., Armenio, V. & De Marchis, M. 2008 The effect of the slope of irregularly distributed roughness elements on turbulent wall-bounded flows. *Journal of Fluid Mechanics* **613**, 385–394.

Nugroho, B., Hutchins, N. & Monty, J. P. 2013 Large-scale spanwise periodicity in a turbulent boundary layer induced by highly ordered and directional surface roughness. *International Journal of Heat and Fluid Flow* **41**, 90–102.

Oeffner, Johannes & Lauder, George V. 2012 The hydrodynamic function of shark skin and two biomimetic applications. *Journal of Experimental Biology* **215** (5), 785–795.

Park, Seong-Ryong & Wallace, James M 1994 Flow Alteration and Drag Reduction by Riblets in a Turbulent Boundary Layer. *AIAA JOURNAL* **32** (1).

Quinn, Daniel B., Lauder, George V. & Smits, Alexander J. 2014 Scaling the propulsive performance of heaving flexible panels. *Journal of Fluid Mechanics* **738**, 250–267.

R García-Mayoral, J Jiménez 2011 Drag reduction by riblets. *Philos Trans R Soc A* **369** (1940), 1412.

Rouhi, Amirreza, Endrikat, Sebastian, Modesti, Davide, Sandberg, Richard D, Oda, Takuo, Tanimoto, Koichi, Hutchins, Nicholas & Chung, Daniel 2022 Riblet-generated flow mechanisms that lead to local breaking of Reynolds analogy. *J. Fluid Mech* **951**, 45.

Saadat, M., Fish, F. E., Domel, A. G., Di Santo, V., Lauder, G. V. & Haj-Hariri, H. 2017 On the rules for aquatic locomotion. *Physical Review Fluids* **2** (8), 083102.

Santos, Leonardo M, Lang, Amy, Wahidi, Redha, Bonacci, Andrew, Devey, Sean,

Parsons, Jacob, Santos, Leonardo M, Lang, Amy, Wahidi, Redha, Bonacci, Andrew, Gautam, Sashank, Devey, Sean & Parsons, Jacob 2021 Passive Separation Control of Shortfin Mako Shark Skin in a Turbulent Boundary Layer. *Experimental Thermal and Fluid Science* p. 110433.

Schlichting, H. 1936 Experimentelle Untersuchungen zum Rauhigkeitsproblem. *Ingenieur-Archiv* **7** (1), 1–34.

Schnipper, Teis, Andersen, Anders & Bohr, Tomas 2009 Vortex wakes of a flapping foil. *Journal of Fluid Mechanics* **633**, 411–423.

Thekkethil, Namshad, Sharma, Atul & Agrawal, Amit 2018 Unified hydrodynamics study for various types of fishes-like undulating rigid hydrofoil in a free stream flow. *Physics of Fluids* **30** (7), 077107.

Triantafyllou, G. S., Triantafyllou, M. S. & Grosenbaugh, M. A. 1993 Optimal Thrust Development in Oscillating Foils with Application to Fish Propulsion. *Journal of Fluids and Structures* **7** (2), 205–224.

Triantafyllou, M. S., Triantafyllou, G. S. & Gopalkrishnan, R. 1991 Wake mechanics for thrust generation in oscillating foils. *Physics of Fluids A: Fluid Dynamics* **3** (12), 2835.

Vanderwel, Christina & Ganapathisubramani, Bharathram 2015 Effects of spanwise spacing on large-scale secondary flows in rough-wall turbulent boundary layers. *Journal of Fluid Mechanics* **774**, R2.

Von Deyn, Lars H, Gatti, Davide, Frohnapfel, Bettina, Von Deyn, L H, Gatti, D & Frohnapfel, B 2022 From drag-reducing riblets to drag-increasing ridges. *J. Fluid Mech* **951**, 16.

Walsh, M. 1982 Turbulent boundary layer drag reduction using riblets. *AIAA* .

Wen, Li, Weaver, James C. & Lauder, George V. 2014 Biomimetic shark skin: design, fabrication and hydrodynamic function. *Journal of Experimental Biology* **217** (10), 1656–1666.

Weymouth, G. D. & Yue, Dick K.P. 2011 Boundary data immersion method for Cartesian-grid simulations of fluid-body interaction problems. *Journal of Computational Physics* **230** (16), 6233–6247.

Zurman-Nasution, A. N., Ganapathisubramani, B. & Weymouth, G. D. 2020 Influence of three-dimensionality on propulsive flapping. *Journal of Fluid Mechanics* **886**.

## Appendix A. Convergence

We tested resolutions of increasing powers of two for two surfaces where $\lambda = 1/16, 1/52$ (figure 10). For figure 10a we measured the error against the value at the highest resolution, which contained $2.4 \times 10^9$ grid cells. The pressure-based thrust $\overline{C_T}$ oscillates around a zero mean, and so we measure the error in $\overline{C_T^2}$. We converge to below 4% error for both surfaces before our working resolution at the lowest limit of $\Delta x = 0.004$. Further, figure 10b shows that the time history of $C_T$ converges before our working resolution also.

Figure 11 shows the convergence of the integral quantity of the x-vorticity magnitude for the two surfaces where $\lambda = 1/16, 1/52$. We measure $\int |\omega_x| dV$ because it is zero for the two-dimensional, smooth cases and, therefore, allows us to quantify the grid independence of the bump contribution to the flow. Again, we converged to within a reasonable limit at our working resolution of $\Delta x = 0.004$.

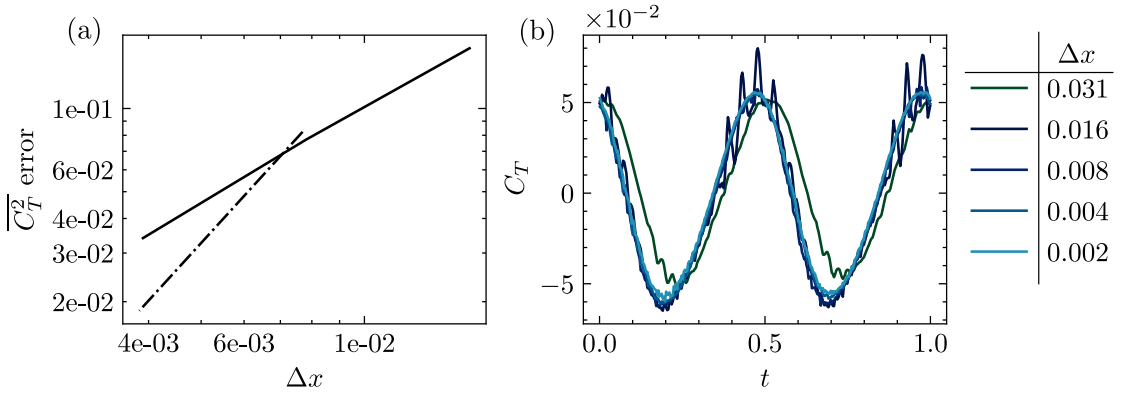


Figure 10: This figure shows the convergence of the thrust for (a), the averages where $\lambda = 1/16$ (solid line), and $\lambda = 1/52$, (dash-dot line), and (b) (colour online) a phase averaged cycle where $\lambda = 1/16$.

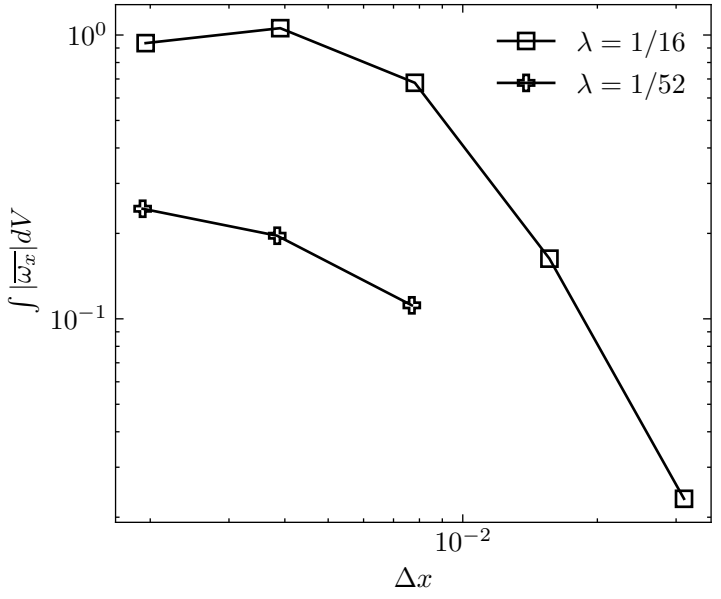


Figure 11: This figure shows the convergence of the $\int |\overline{\omega_x}| dV$ with simulation fidelity.